Self-Calibrating Position Measurements Applied to Imperfect Hall Sensors

Van Meer, Max; Van Noije, Marijn; Tiels, Koen; Evers, Enzo; Blanken, Lennart; Witvoet, Gert; Oomen, Tom

DOI
10.1016/j.ifacol.2025.10.143

Publication date
2025

Document Version
Final published version

Published in
IFAC-PapersOnline

Available online at www.sciencedirect.com

ScienceDirect

IFAC PapersOnline CONFERENCE PAPER ARCHIVE

IFAC PapersOnLine 59-17 (2025) 79–84

Self-Calibrating Position Measurements: Applied to Imperfect Hall Sensors [1]

Max van Meer * **Marijn van Noije** * **Koen Tiels** * **Enzo Evers** ** **Lennart Blanken** *,** **Gert Witvoet** *,*** **Tom Oomen** *,****

* *Control Systems Technology section, Department of Mechanical Engineering, Eindhoven University of Technology, The Netherlands (e-mail: m.v.meer@tue.nl).*

** *Mechatronics department, Sioux Technologies B.V., Eindhoven, The Netherlands.*

*** *Department of Optomechatronics, TNO, Delft, The Netherlands.*

**** *Delft Center for Systems and Control, Delft University of Technology, Delft, The Netherlands.*

Abstract: Linear Hall sensors are a cost-effective alternative to optical encoders for measuring the rotor positions of actuators, with the main challenge being that they exhibit position-dependent inaccuracies resulting from manufacturing tolerances. This paper develops a data-driven calibration procedure for linear analog Hall sensors that enables accurate online estimates of the rotor angle without requiring expensive external encoders. The approach combines closed-loop data collection with nonlinear identification to obtain an accurate model of the sensor inaccuracies, which is subsequently used for online compensation. Simulation results show that when the flux density model structure is known, measurement errors are reduced to the sensor noise floor, and experiments on an industrial setup demonstrate a factor of 2.6 reduction in the root-mean-square measurement error. These results confirm that Hall sensor inaccuracies can be calibrated even when no external encoder is available, improving their practical applicability.

Keywords: Mechatronic Systems, Calibration, Hall Sensors, Nonlinear Identification, Position Measurements

1. INTRODUCTION

Accurate position measurements are key in high-performance actuators for applications such as semiconductor manufacturing or optical satellite communication (Mack, 2007; Kramer et al., 2020). These actuators must meet strict positioning requirements, often in the micrometer or microradian range, to achieve accurate control performance (Oomen, 2018). Meanwhile, the demand for mass-produced solutions has created a need for more economical sensors that still meet these requirements.

Figure 1 depicts a set of Linear Hall sensors on a rotor, which offer a promising alternative to costly, high-resolution encoders for electric actuators. A Hall sensor outputs a voltage proportional to the local magnetic flux density, which can be processed to estimate the rotor angle (Ramsden, 2006; Liu et al., 2008). Compared to high-end encoders, linear Hall sensors are cheaper, more compact, and easier to integrate in large volumes.

Hall-based sensing nevertheless suffers from position-dependent inaccuracies due to uneven magnetization, manufacturing tolerances, and sensor misalignments. These imperfections introduce periodic measurement errors, which can lead to degraded control performance and parasitic vibrations (Pan et al., 2015; Xiao et al., 2007), see Figure 2. Calibration is thus required to eliminate the resulting ripples in the estimated rotor position.

Existing approaches to sensor calibration use external sensors or automated test benches to obtain a ground truth (Dresscher et al., 2019; van Meer et al., 2023), which effectively corrects measurement errors. Alternatively, filter-based methods (Xiao et al., 2007; Jung et al., 2010) successfully suppress Hall-induced vibrations online using feedback. Other methods avoid external sensors by using measurement models (Du et al., 2018; Kim et al., 2016) or extended Kalman filters (Yong Zhao and Westwick, 2004). Still, these methods have their limitations. Reliance on external sensors greatly increases the cost of calibration in a mass-production setting, even with automated test benches. Moreover, filter-based methods limit control bandwidth by introducing phase lag. Existing methods avoiding external position sensors instead rely on rough position estimates, assume ideal sensor placement or are too computationally demanding for low-cost hardware.

Although these methods improve measurement accuracy, no procedure relies solely on analog Hall signals and actua-

[1] This work is part of the research programme VIDI with project number 15698, which is (partly) financed by the Netherlands Organisation for Scientific Research (NWO). In addition, this research has received funding from the ECSEL Joint Undertaking under grant agreement 101007311 (IMOCO4.E). The Joint Undertaking receives support from the European Union's Horizon 2020 research and innovation program.

10.1016/j.ifacol.2025.10.143

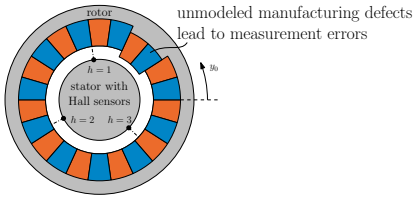

Fig. 1. Experimental setup: Linear Hall sensors h on the stator measure flux density d_h from rotor-mounted magnets. Blue and red blocks indicate south and north poles. The flux density depends on the rotor position y_0, but reconstructing $y \approx y_0$ is complicated by unmodeled manufacturing defects. Stator windings are omitted from the scheme for simplicity.

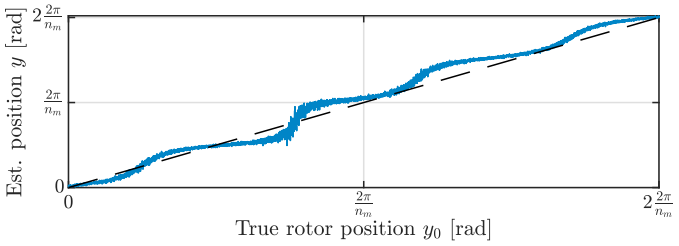

Fig. 2. Illustrative example of a position-dependent measurement inaccuracy, plotted along two out of n_m pole-pairs. When the position is reconstructed (—) from flux density signals while neglecting higher order harmonics, the estimate of true rotor angle (- -) is not accurate and potentially varies along each pole pair.

tor torque commands while avoiding strict assumptions on sensor placement. Therefore, this paper aims to calibrate analog linear Hall sensors through closed-loop experiments and simulation error minimization. No external angle sensor or expensive test setup is needed, making the method suitable for cost-sensitive, large-scale production.

The main contributions are as follows.

- C1 A closed-loop identification and calibration strategy is developed that relies solely on Hall measurements and torque commands while capturing higher-order harmonic distortions in the flux density.
- C2 Simulation results show that the method accurately estimates the rotor angle without external position information.
- C3 Experiments demonstrate improved measurement accuracy on an industrial setup.

This paper is structured as follows. Section 2 formalizes the problem. Section 3 describes the calibration approach. Sections 4 and 5 demonstrate its effectiveness in simulations and experiments. Finally, Section 6 provides conclusions.

2. PROBLEM DESCRIPTION

This section describes the challenges associated with reconstructing the rotor position of an electric motor using Hall sensor measurements.

2.1 Experimental setup: Hall sensors on an electric motor

Consider an electric motor with linear time-invariant (LTI) torque dynamics given by

$$y_0(s) = G(s)T(s), \tag{1}$$

where $y_0 \in \mathbb{R}$ represents the true rotor position,

$$T(s) = T_u(s) + T_d(s) \tag{2}$$

is the applied torque consisting of a control action T_u and external disturbances T_d, and $G(s)$ is a transfer function with Laplace operator s. The rotor contains n_m pole pairs that generate a position-dependent magnetic field. Three Hall sensors $h \in \{1, 2, 3\}$ are mounted on the stator, spaced approximately 120° apart in electrical angle. Neglecting dependence on temperature, each sensor measures a voltage d_h assumed proportional to the local magnetic flux density, given by

$$d_h(t_k) = g_h(y_0(t_k)) + v_h(t_k), \tag{3}$$

where $t_k = T_s k$ with sample time T_s and discrete-time sample number k. Here, $g_h(y_0)$ describes the periodic relationship between rotor position y_0 and scaled flux density with $y_0 = 0$ at t_0, and $v_h(t_k)$ is zero-mean, independent sensor noise with variance σ_h^2. The series connection of linear system $G(s)$ and nonlinear functions $g_h(y_0)$ is recognized as a single-input multi-output Wiener system in literature (Westwick and Verhaegen, 1996).

2.2 Computing the rotor position from Hall sensor data

Estimates $y \approx y_0$ can be reconstructed from the Hall sensor measurements d_h if the mapping

$$\mathbf{g}(y_0) = [g_1(y_0)\ g_2(y_0)\ g_3(y_0)]^\top \tag{4}$$

has a left inverse. This is the case if and only if $\mathbf{g}(y_0)$ is injective, i.e., any unique flux density vector $\mathbf{d} = \mathbf{g}(y_0)$ must correspond to exactly one rotor position y_0. This is not the case on the whole domain $y_0 \in \mathbb{R}$: not only is $\mathbf{g}(y_0)$ periodic with mechanical period 2π, it is also periodic with period $\frac{2\pi}{n_m}$ if the pole-pairs are placed axisymmetrically.

This issue is overcome by including prior information about the specific period that $y_0(t_k)$ is currently in, e.g., by using the previous position estimate

$$\phi \triangleq y(t_{k-1}) \tag{5}$$

and assuming a sufficiently small T_s. In this case, $\mathbf{g}(y_0)$ is not required to be injective on the whole domain $y_0 \in \mathbb{R}$, but only in a domain $\mathcal{Y}_\phi$ smaller than the periodicity of $\mathbf{g}(y_0)$, centered around ϕ:

$$\mathcal{Y}_\phi = \left\{ y_0 \mid \phi - \frac{\pi}{n_m} < y_0 < \phi + \frac{\pi}{n_m} \right\}. \tag{6}$$

Within this domain, the estimate y of the true position y_0 follows from a function f_ϕ satisfying

$$f_\phi(\mathbf{g}(y_0)) = y_0, \quad \forall y_0 \in \mathcal{Y}_\phi. \tag{7}$$

Thus, $\phi \triangleq y(t_{k-1})$ in (7) acts as a history-capturing variable that enables reconstruction of the mechanical rotor position y_0 despite periodic flux densities.

Since $\mathbf{g}(y_0)$ is unknown, (7) cannot be used for designing the left inverse f_ϕ. Instead, f_ϕ is designed using a model $\hat{\mathbf{g}}(y_0) \approx \mathbf{g}(y_0)$ to satisfy the condition

$$f_\phi(\hat{\mathbf{g}}(y_0)) = y_0, \quad \forall y_0 \in \mathcal{Y}_\phi, \tag{8}$$

where model mismatch would lead to estimation error $y_0 - f_\phi(\hat{\mathbf{g}}(y_0))$. The next section addresses the importance of accurately modeling $\hat{\mathbf{g}}(y_0) \approx \mathbf{g}(y_0)$.

Algorithm 1 Data-driven calibration of Hall sensors

Require: Controller $C(s)$, BLA $\hat{G}_{\text{BLA}}(q)$, reference $r(t_k)$.
1: Track $r(t_k)$ in closed-loop using $f_\phi = f_\phi^{\text{init}}$ in (9), store $\mathbf{d}(t_k)$ and $y(t_k)$ in $\mathcal{D}$. (Section 3.1)
2: Set $\hat{G}_{\text{BLA}}(q) \leftarrow \hat{G}_{\text{BLA}}(q)/\hat{c}$ with (23). (Section 3.3)
3: Solve (14) to obtain $\hat{\mathbf{g}}_{\theta^\star}$. (Section 3.1)
4: Create $f_\phi^\star$ using (20). (Section 3.2)
5: **return** Reconstruction function $f_\phi^\star$.

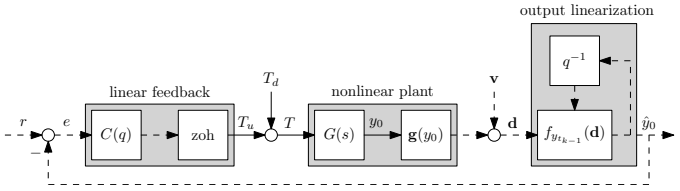

Fig. 3. Closed-loop data collection scheme. Rotor position estimates $y \approx y_0$ are reconstructed from flux density signals $\mathbf{d}$ and are used for position feedback control, suppressing external disturbances T_d. Solid and dashed lines represent continuous-time and discrete-time signals, respectively.

2.3 Consequences of incorrect reconstruction

Imperfect modeling of $\mathbf{g}(y_0)$ leads to periodic errors in the reconstructed rotor position y, resulting in ripples that degrade tracking performance and cause vibrations. Assuming Hall signals are purely sinusoidal is inadequate due to manufacturing tolerances, uneven magnetization, and misaligned sensors. These imperfections introduce higher-order harmonics and cause measurement inaccuracy when left unaddressed; see Figure 2. This shows the need for a model $\hat{\mathbf{g}}(y_0)$ to accurately capture flux density behavior.

2.4 Problem definition

The aim is to obtain accurate rotor position estimates $y \approx y_0$ from Hall sensor measurements $\mathbf{d}$. No external position sensors are available for calibration except for validation purposes, and the solution must be robust to external disturbances and implementable on low-cost embedded hardware. This involves two main tasks:

(1) Identify an accurate flux density model $\hat{\mathbf{g}}(y_0)$ based on the measurements $\mathbf{d}$ and applied torque T.
(2) Design an f_ϕ satisfying (8).

3. SELF-CALIBRATING HALL SENSORS

This section describes the developed calibration approach for Hall-based rotor position estimation. Section 3.1 presents flux density modeling, experiment design, and identification. Section 3.2 details the reconstruction function, and Section 3.3 covers implementation. Algorithm 1 summarizes the procedure.

3.1 Modeling the flux density function $\mathbf{g}$

The first step involves identifying an accurate model $\hat{\mathbf{g}}(y_0)$ of the flux density function $\mathbf{g}(y_0)$ from measured data. The modeling process consists of three key steps: experiment design, model structure definition, and identification. These steps are described below.

Experiment design Data is collected in closed-loop, using a feedback controller $C(s)$ for safety and for mitigation of disturbances T_d. During data collection, an initial reconstruction function f_ϕ^{init} estimates the rotor position to facilitate linear position feedback. This function combines a Clarke transformation and the atan2 function to approximate the rotor position based on the Hall sensor measurements $\mathbf{d} = [d_1, d_2, d_3]^\top$ (Hussain and Toliyat, 2016):

$$y(t_k) = f^{\text{init}}_{y_{t_{k-1}}}(\mathbf{d}(t_k))$$
$$f^{\text{init}}_{y_{t_{k-1}}}(\mathbf{d}(t_k)) := \frac{1}{n_m}\left(\Gamma\left(\text{atan2}\left(\tilde{d}_2(t_k), \tilde{d}_1(t_k)\right), y_{t_{k-1}}\right)\right), \tag{9}$$

with $\Gamma : \mathbb{R} \times \mathbb{R} \to \mathbb{R}$ an unwrapping function given by

$$\Gamma(y_{t_k}, y_{t_{k-1}}) := y_{t_{k-1}} + \text{mod}\left(y_{t_k} - y_{t_{k-1}} + \pi, 2\pi\right) - \pi, \tag{10}$$

and $\tilde{\mathbf{d}} = \mathbf{C}\mathbf{d}$ with $\mathbf{C}$ the Clarke transformation matrix:

$$\mathbf{C} = \frac{2}{3}\begin{bmatrix} 1 & -\frac{1}{2} & -\frac{1}{2} \\ 0 & \frac{\sqrt{3}}{2} & -\frac{\sqrt{3}}{2} \\ \frac{1}{2} & \frac{1}{2} & \frac{1}{2} \end{bmatrix}. \tag{11}$$

This initial f_ϕ^{init} satisfies (7) if $\mathbf{g}(y_0)$ consists solely of three pure sinusoids shifted by 120°, without higher-order harmonics. In practice, however, sensor misalignments and uneven magnetization give rise to harmonic distortions that make (9) only an approximation $y(t_k) \approx y_0(t_k)$.

Despite these inaccuracies, the approximate reconstruction is sufficient to enable closed-loop control, as shown in Figure 3. The feedback controller C suppresses external disturbances T_d and ensures that the approximated rotor position tracks a ramp reference. Perfect reference tracking is not achieved because of the higher harmonics in $\mathbf{g}$, but this is not required for identification; the feedback controller need only suppress T_d in T. Section 3.3 addresses the reference and controller design. During experiments, the N samples of $\mathbf{d}(t_k)$ and $y(t_k)$ are stored in the dataset $\mathcal{D}$ for use in identification.

Model structure The flux density function $\mathbf{g}(y_0)$ is parametrized linear in the parameters for simplicity:

$$\hat{\mathbf{g}}_{\boldsymbol{\theta}}^\top(y_0) = \boldsymbol{\psi}(y_0)\boldsymbol{\theta}, \tag{12}$$

where $\boldsymbol{\theta} \in \mathbb{R}^{n_\theta}$ are model parameters, and

$$\boldsymbol{\psi}(y_0) = \mathbf{I}_3 \otimes \boldsymbol{\beta}(y_0), \tag{13}$$

with $\otimes$ the Kronecker product and $\boldsymbol{\beta} : \mathbb{R} \to \mathbb{R}^{1\times m}$ a periodic basis function, such as a Fourier basis or a periodic kernel function (Rasmussen and Williams, 2006). The order m can be chosen by analyzing the harmonic content of data $\mathbf{d}(t_k)$.

Identification The parameters $\boldsymbol{\theta}$ are identified by solving a simulation error minimization (SEM) problem. The cost function $J(\boldsymbol{\theta})$ is defined as the squared 2-norm of the difference between the measured flux density $\mathbf{d} \in \mathcal{D}$ and a simulated flux density $\mathbf{d}_{\boldsymbol{\theta}}^{\text{sim}}$:

$$\min_{\boldsymbol{\theta}} J(\boldsymbol{\theta}),$$
$$J(\boldsymbol{\theta}) = \sum_{k=1}^{N}\left(\mathbf{d}(t_k) - \mathbf{d}_{\boldsymbol{\theta}}^{\text{sim}}(t_k)\right)^\top\left(\mathbf{d}(t_k) - \mathbf{d}_{\boldsymbol{\theta}}^{\text{sim}}(t_k)\right). \tag{14}$$

Here, $\mathbf{d}_{\boldsymbol{\theta}}^{\text{sim}}(t_k)$ is computed using the state and output equations of the closed-loop system, incorporating a Best Linear Approximation (BLA) $\hat{G}_{\text{BLA}}(q) \approx G(q)$, detailed in Section 3.3, and the model $\hat{\mathbf{g}}_{\boldsymbol{\theta}}(y_0)$. These equations are:

$$\begin{aligned}
\mathbf{d}_{\boldsymbol{\theta}}^{\text{sim}}(t_k) &= \hat{\mathbf{g}}_{\boldsymbol{\theta}}(y_0^{\text{sim}}(t_k)),\\
y_{0,\boldsymbol{\theta}}^{\text{sim}}(t_k) &= \mathbf{C}_{G_{\text{BLA}}}\mathbf{x}_{G_{\text{BLA}},\boldsymbol{\theta}}(t_k),\\
\mathbf{x}_{G_{\text{BLA}},\boldsymbol{\theta}}(t_{k+1}) &= \mathbf{A}_{G_{\text{BLA}}}\mathbf{x}_{G_{\text{BLA}},\boldsymbol{\theta}}(t_k) + \mathbf{B}_{G_{\text{BLA}},\boldsymbol{\theta}}T_{\boldsymbol{\theta}}^{\text{sim}}(t_k),\\
T_{\boldsymbol{\theta}}^{\text{sim}}(t_k) &= \mathbf{C}_C\mathbf{x}_{C,\boldsymbol{\theta}}(t_k) + \mathbf{D}_C e_{\boldsymbol{\theta}}^{\text{sim}}(t_k),\\
\mathbf{x}_{C,\boldsymbol{\theta}}(t_{k+1}) &= \mathbf{A}_C\mathbf{x}_{C,\boldsymbol{\theta}}(t_k) + \mathbf{B}_C e_{\boldsymbol{\theta}}^{\text{sim}}(t_k),\\
e_{\boldsymbol{\theta}}^{\text{sim}}(t_k) &= r(t_k) - y_{\boldsymbol{\theta}}^{\text{sim}}(t_k),\\
y_{\boldsymbol{\theta}}^{\text{sim}}(t_k) &= f^{\text{init}}_{y_{\boldsymbol{\theta}}^{\text{sim}}(t_{k-1})}(\mathbf{d}_{\boldsymbol{\theta}}^{\text{sim}}(t_k)), \quad \forall k \in \{1,\dots,N\}
\end{aligned} \tag{15}$$

with zero initial conditions. Here, $\mathbf{A}_{G_{\text{BLA}}}$, $\mathbf{B}_{G_{\text{BLA}}}$, and $\mathbf{C}_{G_{\text{BLA}}}$ represent the state and output matrices of the BLA, while $\mathbf{A}_C$, $\mathbf{B}_C$, $\mathbf{C}_C$, and $\mathbf{D}_C$ describe the discrete-time controller. Problem (14) is solved using an interior-point method with approximate gradients, starting at an initial estimate $\boldsymbol{\theta}_0$ corresponding to pure sinusoids, i.e., the inverse of f^{init}. Since the cost is non-convex, $\boldsymbol{\theta}^\star$ corresponds to a local minimum.

3.2 Designing a reconstruction function $f_\phi^\star$

With the flux density model $\hat{\mathbf{g}}(y_0)$ available, a reconstruction function $f_\phi^\star$ is designed to estimate the rotor position while compensating for inaccuracies in the initial reconstruction function f_ϕ^{init}. First, a lookup table is defined on a grid of M equidistant points $y_{0,i}$ within the interval $[0, 2\pi)$. Using the model $\hat{\mathbf{g}}(y_0)$, the corresponding outputs of the initial reconstruction function f_ϕ^{init} are computed:

$$\hat{y}_i = f^{\text{init}}_{y_{0,i}}(\hat{\mathbf{g}}_{\boldsymbol{\theta}}(y_{0,i})), \quad i \in \{1,\dots,M\}. \tag{16}$$

The additive measurement error caused by f_ϕ^{init} on this grid is then estimated as

$$\hat{\eta}_i^{\text{LUT}} := y_{0,i} - \hat{y}_i, \quad i \in \{1,\dots,M\}. \tag{17}$$

Next, a piecewise-linear correction function $\hat{\eta}^{\text{LUT}}(\hat{y})$ is defined to interpolate between the points $(\hat{y}_i, \eta_i^{\text{LUT}})$. For a given $\hat{y}$, the index i is determined such that:

$$i = \text{argmin}_i \left\{\hat{y} \in [\hat{y}_i, \hat{y}_{i+1})\right\}, \tag{18}$$

where the interpolation wraps around at the boundaries, i.e., $\hat{y}_{M+1} = \hat{y}_1$ and $\eta_{M+1}^{\text{LUT}} = \eta_1^{\text{LUT}}$. The piecewise-linear interpolation is then computed as:

$$\eta^{\text{LUT}}(\hat{y}) = \hat{\eta}_i^{\text{LUT}} + \frac{\hat{y} - \hat{y}_i}{\hat{y}_{i+1} - \hat{y}_i}\left(\hat{\eta}_{i+1}^{\text{LUT}} - \hat{\eta}_i^{\text{LUT}}\right). \tag{19}$$

Finally, the reconstruction function $f_\phi^\star$ is defined to compensate for the additive measurement error, yielding:

$$f_\phi^\star(\mathbf{d}) = f_\phi^{\text{init}}(\mathbf{d}) + \eta^{\text{LUT}}\left(f_\phi^{\text{init}}(\mathbf{d})\right). \tag{20}$$

This adjustment corrects the periodic inaccuracies in f_ϕ^{init} in a computationally lightweight manner, improving the accuracy of rotor position estimation. Note that this simple approach requires (16) to be bijective. If it is not, a different approach to designing $f_\phi^\star$ is required that avoids f_ϕ^{init} altogether. The next section discusses relevant implementation aspects.

3.3 Implementation aspects

Several practical considerations are important for implementing the developed method, as detailed next.

Control and reference design The closed-loop data collection in Section 3.1.1 uses a feedback controller $C(s)$ to suppress external disturbances T_d on total torque T. To mitigate these disturbances, the sensitivity (Franklin et al., 1994) must be low in magnitude. With the nonlinear function $\mathbf{g}$ approximately linearized by f_ϕ^{init} in Figure 3, the sensitivity is given by

$$S(s) = \frac{T(s)}{T_d(s)} \;\approx\; \frac{1}{1 + G(s)\,C(s)}. \tag{21}$$

Including an integrator in $C(s)$ ensures that the sensitivity is low in magnitude at low frequencies and effectively suppresses slowly varying disturbances. A slow ramp reference from 0 to $2\pi n$ rad with $n \in \mathbb{R}_{\geq 1}$ places any position-dependent disturbances in this low-frequency range where they are well attenuated.

Obtaining a Best Linear Approximation The BLA $\hat{G}_{\text{BLA}}(q)$ required for Step 3 in Algorithm 1 is identified up to an unknown constant in closed-loop using the approach described in Pintelon and Schoukens (2012, Section 3.8), averaging over multiple realizations of random-phase multisine reference signals. This yields

$$\hat{G}_{\text{BLA}}(q) = cG(q), \tag{22}$$

with $c \in \mathbb{R}$. To correct for this mismatch, $\hat{c} \approx c$ is estimated from data $\mathcal{D}$ by minimizing

$$\hat{c} = \arg\min_c \left(y_{\boldsymbol{\theta}_0,c}^{\text{sim}}(t_{p_{\text{sim}}}) - y^{\text{dat}}(t_{p_{\text{dat}}})\right)^2, \tag{23}$$

where $y_{\boldsymbol{\theta}_0,c}^{\text{sim}}(t_{p_{\text{sim}}})$ follows from (15) using a scaled BLA $\tilde{\mathbf{B}}_{G_{\text{BLA}}} = c\mathbf{B}_{G_{\text{BLA}}}$, and $y^{\text{dat}} \in \mathcal{D}$. Moreover, t_p is the time instance of the last full rotation:

$$p_\iota := \arg\max_{p_\iota} \left\{y^\iota(t_{p_\iota}) = 2\pi n \mid n \in \mathbb{N}, t_{p_\iota} \leq t_N\right\}, \tag{24}$$

for both $\iota \in \{\text{sim}, \text{dat}\}$. The estimate $\hat{c} \approx c$ in (23) relies on $\mathbf{g}(y_0)$ being periodic with known period 2π. Indeed, the number of full rotations of the rotor is independent of the shape of the measurement errors, so any mismatch between simulation (15) and the data must be attributed to incorrect scaling of the BLA. Once $\hat{c} \approx c$ is estimated, it is used to compensate the BLA in Step 2 of Algorithm 1, before the nonlinear identification step.

4. SIMULATION RESULTS

This section demonstrates the performance of the developed calibration approach on a simulation example.

4.1 Simulation setup

Consider an example motor with $n_m = 11$ permanent magnets and linear dynamics

$$G(s) := \frac{y_0(s)}{T(s)} = \frac{1.663 \cdot 10^5}{s^3 + 632.6\,s^2 + 2702\,s}\exp\left(1.2 \cdot 10^{-4} s\right). \tag{25}$$

Moreover, $\mathbf{g}(y_0)$ is parametrized by a Fourier basis $\boldsymbol{\beta}(y_0) \in \mathbb{R}^{1\times(2n_h+1)}$. The first element is $\beta_1(y_0) = 1$, and

$$\begin{aligned}
&\beta_{1+i}(y_0) = \sin\left(y_0\, h_{\lceil i/2 \rceil}\right),\\
&\beta_{2+i}(y_0) = \cos\left(y_0\, h_{\lceil i/2 \rceil}\right),\\
&\qquad \forall i \in \{\, i \in \mathbb{N} \mid i \text{ odd}, 1 \leq i \leq 2n_h - 1\},
\end{aligned} \tag{26}$$

with harmonics $\mathbf{h} = [\,1, \dots, 11\,]^\top$. A parameter vector $\boldsymbol{\theta}$ is chosen so that each permanent magnet has a slightly

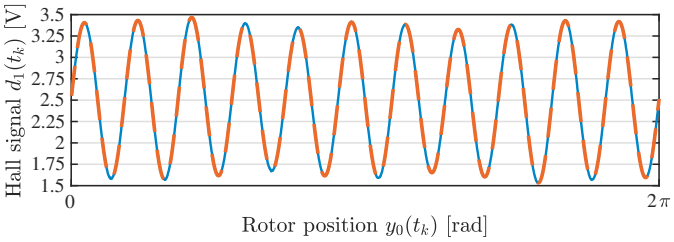

Fig. 4. Simulation example. The first Hall signal $d_1(t_k)$ (—) is approximately periodic with the magnet pitch, with slight variations across magnets. The estimates $\hat{d}_1 = \hat{g}_{1,\boldsymbol{\theta}^\star}(\mathbf{d}(t_k))$ (- -) from the model in Step 3 of Algorithm 1 closely match the true function.

different flux density profile, as Figure 4 shows it is not quite periodic with period $2\pi/n_m$. The flux density signals are sampled at $F_s = 4000$ Hz, each with noise variance $\sigma_h^2 = 7.5 \cdot 10^{-6}$ V. A stabilizing controller is given by

$$C(q) = \frac{2.94q^3 - 3.29q^2 - 2.10q + 2.45}{q^4 - 3.45q^3 + 4.52q^2 - 2.68q + 0.61} \tag{27}$$

and is used in the control scheme in Figure 3.

4.2 Approach

First, a BLA $\hat{G}_{\mathrm{BLA}}(s)$ is measured in closed-loop following the procedure in Section 3.3.2. Algorithm 1 is then applied with model structure (26). During data collection, a reference $r(t_k)$ increases linearly from 0 to 13 rad in 26 s. Problem (14) is solved in two hours on a standard desktop computer, and (16) is verified to be bijective.

4.3 Results

Figure 4 illustrates one of the simulated flux density signals $d_1(t_k)$, together with the estimates $\hat{d}_1(t_k) = \hat{g}_{1,\boldsymbol{\theta}^\star}(y_0^{\mathrm{sim}}(t_k))$. The model $\hat{\mathbf{g}}_{\boldsymbol{\theta}^\star}$ accurately captures the slight flux density variations across the magnets. Figure 5 depicts the estimation error in the rotor angle when using the initial reconstruction f_ϕ^{init} versus the final reconstruction $f_\phi^\star$. The initial reconstruction exhibits a clear periodic error due to unmodeled higher-order harmonics. The final reconstruction $f_\phi^\star$ corrects these structural errors and reduces the error to the sensor noise level. Note that the true rotor position y_0 is only used here for validation; it is not part of the calibration procedure.

These results show that the developed method accurately calibrates Hall sensors without relying on an external reference encoder. As shown next, measurement accuracy is also improved on an industrial setup.

5. EXPERIMENTAL RESULTS

This section validates the approach experimentally.

5.1 Experimental setup

A confidential setup from Sioux Technologies B.V. with a Brushless Direct Current (BLDC) motor is used for experimental validation. The setup follows Figure 1, with a rotor of $n_m = 11$ pole pairs and an external encoder for validation only. Three Hall sensors, spaced approximately 120 electrical degrees apart, are sampled at $F_s = 4000$ Hz. The same feedback controller as in (27) is used.

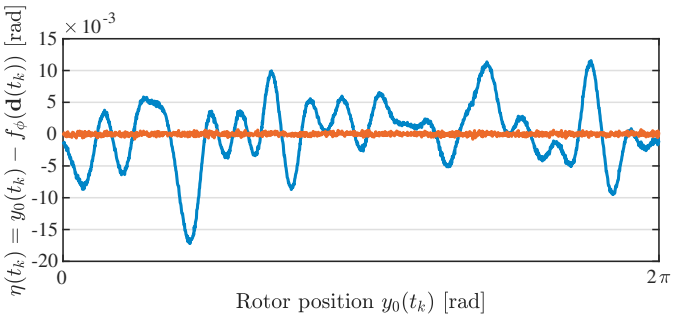

Fig. 5. Measurement error in the simulation. Using the initial $f_\phi^{\mathrm{init}}(\mathbf{d})$ results in a large measurement error (—). Using $f_\phi^\star(\mathbf{d})$ from Algorithm 1 reduces the measurement error down to the noise floor (—).

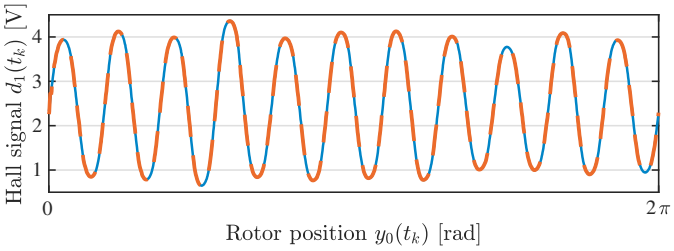

Fig. 6. Experimental data. The measured Hall signal $d_1(t_k)$ (—) repeats roughly with each magnet but shows slight variations. The identified model $\hat{d}_1(t_k) = \hat{g}_{1,\boldsymbol{\theta}^\star}(y_0^{\mathrm{sim}}(t_k))$ (- -) accurately estimates the flux densities without relying on $y_0(t_k)$.

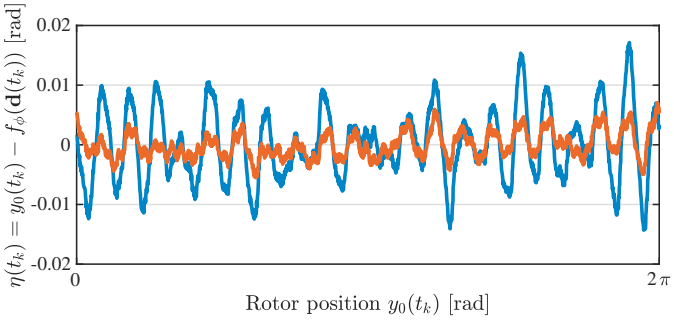

Fig. 7. Measurement error in the experiments, with the external encoder used for validation only. The initial $f_\phi^{\mathrm{init}}(\mathbf{d})$ produces a large error (—). After Algorithm 1, $f_\phi^\star(\mathbf{d})$ achieves a significant reduction (—).

5.2 Approach

As before, a BLA $\hat{G}_{\mathrm{BLA}}(s)$ is identified using the closed-loop approach in Section 3.3.2. The flux density model $\hat{\mathbf{g}}_{\boldsymbol{\theta}}$ is then expressed through a kernel-based basis function $\boldsymbol{\beta}(y_0) : \mathbb{R} \to \mathbb{R}^{1\times m}$, where $m = 400$. A grid of m points $y_{0,j}$ is defined equidistantly in $[\,0, 2\pi)$. The kernel is defined by

$$\boldsymbol{\beta}_j(y_0) = k(y_0, y_{0,j}), \quad k(y, y') = \sigma_f^2 \exp\Big(-\tfrac{1}{2\ell^2}\|\mathbf{x} - \mathbf{x}'\|^2\Big), \tag{28}$$

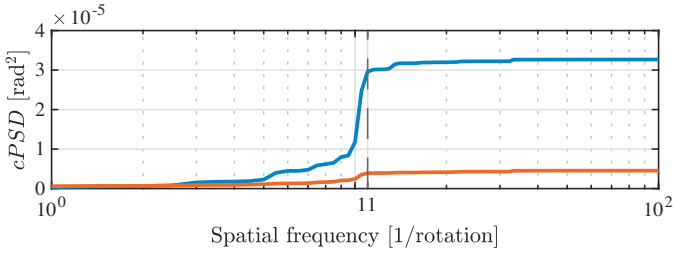

Fig. 8. Cumulative power spectral density of the measurement error. The initial $f_\phi^{\text{init}}(\mathbf{d})$ (—) shows clear periodic content with the spatial frequency $n_m = 11$ corresponding to the magnet count. The final $f_\phi^\star(\mathbf{d})$ (—) corrects for these errors.

where $\mathbf{x} = [\sin(y), \cos(y)]^\top$. Hyperparameters σ_f and ℓ are selected by including them as design variables in (14). The reference $r(t_k)$ is a ramp from 0 to 20 rad over 40 s. Problem (14) is solved in ten hours on a standard desktop computer, and (16) is verified to be bijective.

5.3 Results

Figure 6 shows an example of the measured Hall signal $d_1(t_k)$ and its estimate $\hat{d}_1(t_k) = \hat{g}_{1,\boldsymbol{\theta}^\star}(y_0^{\text{sim}}(t_k))$, where the identified model captures magnet variations. Figure 7 presents the measurement error using the external encoder for validation. The initial reconstruction f_ϕ^{init} results in an RMS error of 5.7 mrad, while the final reconstruction $f_\phi^\star$ compensates for higher-order harmonics, reducing it to 2.2 mrad. The peak $\|\eta\|_\infty$ is reduced by a factor of 2.5.

Figure 8 shows the cumulative power spectral density of the measurement error. Much of the frequency content aligns with the magnet pitch, which the corrected reconstruction significantly suppresses. These results confirm that the calibration method improves rotor position estimation on an industrial setup, achieving a factor of 2.6 improvement in RMS accuracy and a factor of 2.5 in peak error without requiring an external reference encoder.

5.4 Discussion

The residual errors in Figure 7 are presumably caused by nonlinear dynamics that are periodic in y_0 with period 2π, such as cogging, affecting $\mathbf{d}$ and indistinguishable from the contribution of $\mathbf{g}$. A potential solution might be to repeat the data collection process for different angular placements of the motor coils, averaging out this effect. This would require a modular design and involves further research.

Furthermore, the developed two-step approach could potentially be simplified to directly construct f_ϕ from data, avoiding modeling the of $\mathbf{g}$. The current two-step approach is motivated by the expectation that nonlinear identification through simulation-error minimization is more robust to measurement noise on $\mathbf{d}$, yet a more thorough analysis for this choice is desirable.

6. CONCLUSION

The developed method improves measurement accuracy of Hall sensors without using external encoders, improving positioning performance and reducing vibrations cost-effectively for mass production. The simulation error minimization accurately estimates flux density functions, and the resulting compensation function reduces measurement error by a factor of 2.6 on an industrial setup. These findings eliminate the need for expensive test benches and enable low-cost position measurements. Future work will focus on reducing offline computation time through multiple shooting and lower-dimensional model structures, and an extension to Hammerstein systems.

ACKNOWLEDGEMENTS

The authors thank Sioux Technologies B.V. for the developments that led to these results and for their support in carrying out the experiments reported in this paper.

REFERENCES

Dresscher, M., Human, J.D., Witvoet, G., et al. (2019). Key Challenges and Results in the Design of Cubesat Laser Terminals, Optical Heads and Coarse Pointing Assemblies. In *2019 IEEE ICSOS*, 1–6.

Du, S., Hu, J., Zhu, Y., and Zhang, M. (2018). A Hall sensor-based position measurement with on-line model parameters computation for permanent magnet synchronous linear motor. *IEEE Sen. J.*, 18(13), 5245–5255.

Franklin, G., Powell, J.D., and Emami-Naeini, A. (1994). *Feedback Control Of Dynamic Systems*.

Hussain, H.A. and Toliyat, H.A. (2016). Field Oriented Control of tubular PM Linear Motor using linear Hall Effect sensors. In *SPEEDAM 2016*, 1, 1244–1248.

Jung, S., Lee, B., and Nam, K. (2010). PMSM control based on edge field measurements by Hall sensors. In *2010 APEC*, 2002–2006.

Kim, J., Choi, S., Cho, K., and Nam, K. (2016). Position Estimation Using Linear Hall Sensors for Permanent Magnet Linear Motor Systems. *IEEE Trans. Ind. Elec.*, 63(12), 7644–7652.

Kramer, L., Peters, J., Voorhoeve, R., et al. (2020). Novel motorization axis for a Coarse Pointing Assembly in Optical Communication Systems. In *IFAC 2020 World Congr.*, volume 53, 8426–8431.

Liu, X., Zheng, Z., Ye, Y., and Lu, Q. (2008). Position detecting for the air-cored TPMLSM with linear Hall-effect sensors. In *ICEMS 2008*, 1417–1420.

Mack, C. (2007). *Fundamental Principles of Optical Lithography*. Wiley.

Oomen, T. (2018). Advanced motion control for precision mechatronics: Control, identification, and learning of complex systems. *IEEJ J. Ind. Appl.*, 7(2), 127–140.

Pan, S., Commins, P.A., and Du, H. (2015). Tubular linear motor position detection by Hall-effect sensors. In *AUPEC 2015*, 1–5.

Pintelon, R. and Schoukens, J. (2012). *System Identification: A Frequency Domain Approach*. Wiley, 2nd edition.

Ramsden, E. (2006). *Hall-Effect Sensors*. Elsevier, Burlington, 2nd edition.

Rasmussen, C. and Williams, C. (2006). *Gaussian processes for machine learning*. London, England.

van Meer, M., Deniz, E., Witvoet, G., and Oomen, T. (2023). Cascaded Calibration of Mechatronic Systems via Bayesian Inference. In *The 22nd World Congress of the International Federation of Automatic Control*, 3405–3410. Yokohama, Japan.

Westwick, D. and Verhaegen, M. (1996). Identifying MIMO Wiener systems using subspace model identification methods. *Sig. Proc.*, 52(2), 235–258.

Xiao, L., Yunyue, Y., and Zhuo, Z. (2007). Study of the Linear Hall-Effect Sensors Mounting Position for PMLSM. In *2007 ICIEA*, 1175–1178.

Yong Zhao and Westwick, D. (2004). A direct approach to identify closed loop Wiener systems, whose linear dynamics are open-loop unstable. In *ACC 2004*, 1, 4782–4787.